ISSN: 2414-1895 DOI: 10.6919/ICJE.202603_12(3).0011

Plasmon-Enhanced MoS_2 Photodetector Enabled by Lithographically Patterned Au Disk Arrays and an h-BN Tunneling Layer

Yinyin Wang

Guangdong University of Technology, Guangzhou, 510006, China

Abstract

High-performance visible light photodetection holds significant application value in optical communications, imaging, and sensing. Here, we demonstrate a plasmon-enhanced photodetector based on few-layer MoS_2 integrated with Au disk arrays fabricated by direct writing lithography and a monolayer h-BN tunneling layer. The Au disk arrays (diameter: 1.5 μm, period: 2.5 μm, thickness: 40 nm), fabricated by direct writing lithography,offer excellent scalability and position controllability. The monolayer h-BN serves as a tunneling layer that not only prevents direct contact between Au and MoS_2, suppressing dark current and photoluminescence quenching, but also enables the tunneling of plasmon-generated hot electrons into MoS_2. Benefiting from the synergistic effects of near-field optical enhancement, hot electron tunneling injection, and strain-induced band modulation, the device exhibits significantly improved photoelectric conversion efficiency. Under 635 nm illumination at an ultralow power density of 0.01 mW/cm², the device achieves a responsivity of 1384 A/W and a detectivity of 9.73×10^{13} Jones, along with stable and fast photoswitching response featuring rise/fall times of 40 ms/138 ms. Finite-difference time-domain simulations confirm pronounced electric field enhancement at the MoS_2 layer induced by the Au disk arrays. This work provides a feasible design strategy for high-performance and scalable two-dimensional material photodetectors.

Keywords

MoS_2; Plasmonics; Photodetector; Hot electrons.

1. Introduction

Photodetectors have found extensive applications in optical communications, imaging, sensing, and integrated photonics [1, 2]. With the development of next-generation photodetectors, two-dimensional (2D) material-based photodetectors have attracted widespread attention due to their tunable bandgaps, flexible integration capabilities, and compatibility with established fabrication processes [3-5]. Among them, MoS_2, as a representative transition metal dichalcogenide, exhibits layer-dependent bandgaps, high optical absorption coefficients, and excellent environmental stability [6, 7]. Compared with monolayer MoS_2, few-layer MoS_2 maintains high optical absorption while offering superior carrier transport properties and mechanical robustness, making it more suitable for practical device applications [8, 9]. However, the intrinsic optical absorption of few-layer MoS_2 remains insufficient for high-sensitivity detection requirements, and its response bandwidth is fundamentally constrained by the bandgap [10].

To overcome these limitations, various enhancement strategies have been explored, including heterostructure engineering [11-13], doping engineering [14], interface modification [2, 15], and coupling with photonic nanostructures [16-18]. Among these approaches, plasmonic structures have

ISSN: 2414-1895 DOI: 10.6919/ICJE.202603_12(3).0011

emerged as a research hotspot owing to their pronounced near-field enhancement effects, design flexibility, and compatibility with other enhancement strategies [3, 19, 20]. Plasmon-enhanced photodetectors primarily rely on three mechanisms: (i) enhanced optical absorption in 2D materials via localized electric fields generated by plasmons [16, 21]; (ii) injection of high-energy hot electrons produced by non-radiative decay of plasmons into the conduction band of adjacent semiconductors [22-24]; and (iii) strain-induced band structure modulation resulting from conformal coverage of 2D materials over nanostructured surfaces, which extends the response bandwidth [25-27].

Despite extensive research on plasmonic enhancement strategies, the controllable fabrication of plasmonic structures remains a critical challenge hindering practical applications. Traditional electron beam lithography enables high-precision patterning but suffers from high cost and low throughput, making it difficult to meet the demands of large-scale production [4, 28]. Conversely, self-assembly methods allow large-area fabrication,but lack precise control over the position and morphology of plasmonic structures [15]. Therefore, developing fabrication techniques that combine high precision with scalability is of great significance. The direct writing lithography technique employed in this work achieves sub-micrometer patterning accuracy while offering excellent position controllability and reasonable fabrication efficiency [29], providing a viable pathway toward the practical implementation of plasmon-enhanced photodetectors.

Furthermore, direct contact between plasmonic structures and 2D materials leads to Fermi level pinning, exciton quenching, and increased dark current [8, 30]. Inserting an ultrathin insulating layer such as h-BN as a tunneling barrier can effectively suppress dark current while maintaining efficient hot electron injection [30-32].

In this work, we fabricate Au disk arrays using direct writing lithography and integrate them with wet-transferred monolayer h-BN and dry-transferred few-layer MoS_2 to construct a structurally complete plasmon-enhanced photodetector. The device is systematically characterized in terms of its I-V characteristics in the 405-1064 nm range, as well as its photoswitching response, responsivity, and detectivity in the 405-808 nm range. Combined with FDTD simulations and band structure analysis, we elucidate the synergistic enhancement mechanism involving near-field optical enhancement, hot electron injection, and strain effects [20, 26, 29].

2. Result and Discussion

To achieve stable and efficient visible light photodetection, we constructed a plasmon-enhanced photodetector based on few-layer MoS_2 integrated with lithographically patterned Au disk arrays and a monolayer h-BN tunneling layer. Fig. 1a presents a three-dimensional schematic of the device structure, consisting of (from bottom to top) a quartz substrate, direct writing lithographically patterned Au disk arrays (diameter: 1.5 μm, period: 2.5 μm, thickness: 40 nm), a monolayer h-BN tunneling layer, few-layer MoS_2 (thickness: 20-30 nm), and Au source/drain electrodes (10 nm Ti/50 nm Au). This structural design fully leverages the synergistic effects of plasmonic near-field enhancement and hot electron injection, while the h-BN tunneling layer effectively prevents direct contact between Au and MoS_2, suppressing dark current and photoluminescence quenching [30, 32]. Fig. 1b illustrates the device fabrication process flow, which comprises four main steps: direct writing lithography of Au disk arrays, wet transfer of monolayer h-BN, dry transfer of few-layer MoS_2, and direct writing lithography of Au electrodes. The entire fabrication process, based on lithographic techniques, offers excellent scalability and position controllability, laying a foundation for large-scale device applications [4, 28].

Fig. 1c shows an optical microscopy image of a representative fabricated device, where the MoS_2 flake, Au disk arrays, and Au electrodes are clearly distinguishable. The Au disk arrays exhibit uniform arrangement with a diameter of 1.5 μm and a period of 2.5 μm, featuring well-defined edges and no apparent defects. Fig. 1d and 1e present AFM topography images of MoS_2 and corresponding height profiles. Height profile measurements along the white line reveal a MoS_2 thickness of approximately 20 nm, confirming its few-layer nature [8, 9]. The smooth surface facilitates intimate

ISSN: 2414-1895 DOI: 10.6919/ICJE.202603_12(3).0011

contact with the underlying layers. The height profiles also reveal protrusions of the h-BN/MoS_2 stack over the Au disks, indicating conformal contact between the 2D materials and the Au disk arrays. This conformal contact induces local strain in MoS_2, the presence and magnitude of which will be further verified by Raman spectroscopy in Fig. 2b [25, 26].

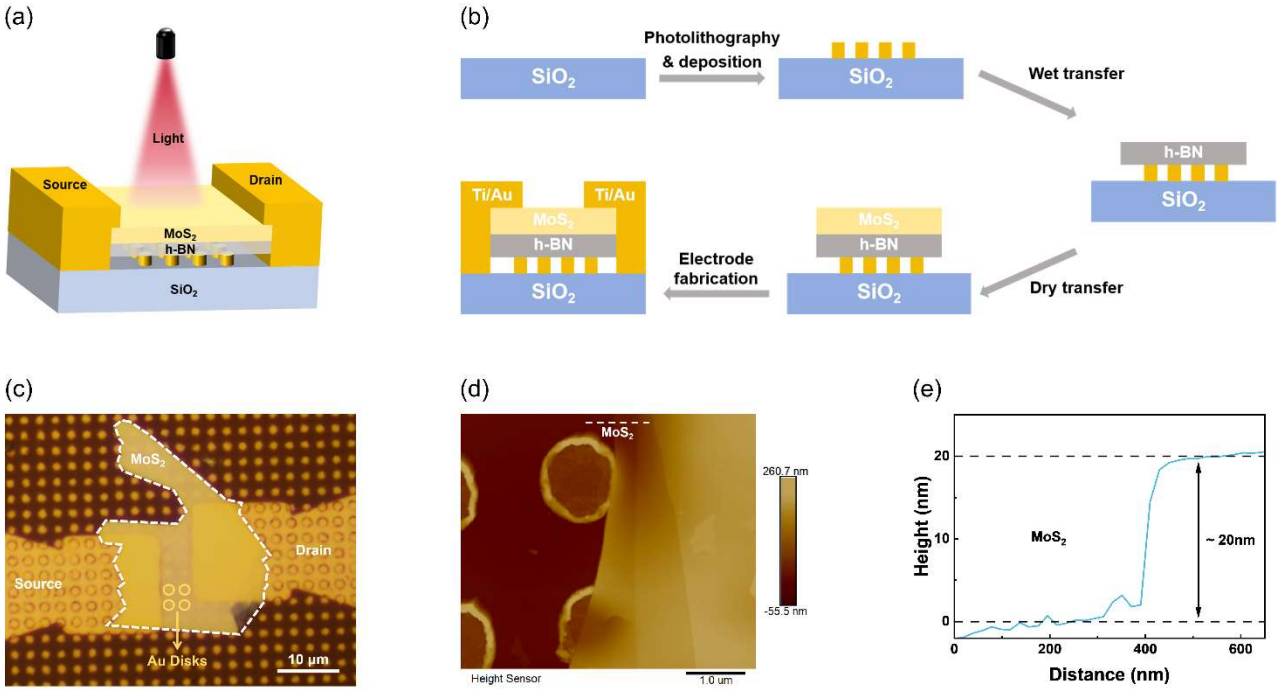

Fig. 1 Structural design and morphology characterization of the device. (a) Schematic illustration of the device structure: SiO_2/Au disk arrays (diameter: 1.5 μm, period: 2.5 μm, thickness: 40 nm)/monolayer h-BN/few-layer MoS_2 (20-30 nm)/Au electrodes. (b) Fabrication process flow: (I) direct writing lithography of Au disk arrays, (II) wet transfer of h-BN, (III) dry transfer of MoS_2, (IV) lithography of electrodes. (c) Optical microscopy image of the fabricated device. (d) AFM image of MoS_2. (e) Height profile of MoS_2, showing a thickness of approximately 20 nm.

Fig. 2a presents the extinction spectra of MoS_2 with and without Au disk arrays. The extinction spectrum reflects the light absorption capability of the sample and serves as an important indicator for evaluating plasmonic resonance characteristics. Simulation results reveal that MoS_2 with Au disk arrays exhibits broadband extinction characteristics in the visible to near-infrared range, with a distinct resonance enhancement peak appearing in the 500-700 nm region that matches well with the 532 nm excitation wavelength. This broadband resonance enables plasmonic enhancement effects at multiple wavelengths [16, 17]. Comparison of the extinction data for MoS_2 with and without Au disk arrays shows that across the 360-1000 nm wavelength range, the extinction of MoS_2 covering the Au disk arrays (blue curve) is significantly higher than that of bare few-layer MoS_2 (black curve), directly confirming the enhanced light absorption of MoS_2 induced by the Au disk arrays [16, 21]. This enhancement is attributed to the near-field effects generated by localized surface plasmons, providing a foundation for subsequent improvements in optoelectronic performance [3, 19].

Fig. 2b shows a comparison of the Raman spectra of MoS_2 with and without Au disk arrays. Both samples exhibit the characteristic Raman peaks of MoS_2: the in-plane vibrational mode E^1_{2g} (~383 cm^{-1}) and the out-of-plane vibrational mode A_{1g} (~408 cm^{-1}), with a peak separation of ~25 cm^{-1}, which is consistent with few-layer MoS_2 [8, 33]. Compared to the sample without Au disk arrays, the Raman peak intensity of MoS_2 on the Au disk arrays is significantly enhanced, further confirming the plasmonic near-field enhancement effect [16, 21]. Meanwhile, a redshift of the characteristic Raman

ISSN: 2414-1895 DOI: 10.6919/ICJE.202603_12(3).0011

peaks is observed, indicating the introduction of tensile strain in MoS_2 during conformal coverage over the Au disk arrays [25, 26]. This strain induces band structure modulation, leading to bandgap narrowing, which contributes to extending the response bandwidth of the device [26, 29]. The simulated extinction spectra and Raman enhancement data corroborate each other, confirming that the Au disk arrays effectively localize the optical field within the MoS_2 layer, providing a structural basis for enhanced light absorption and hot electron generation [16, 17].

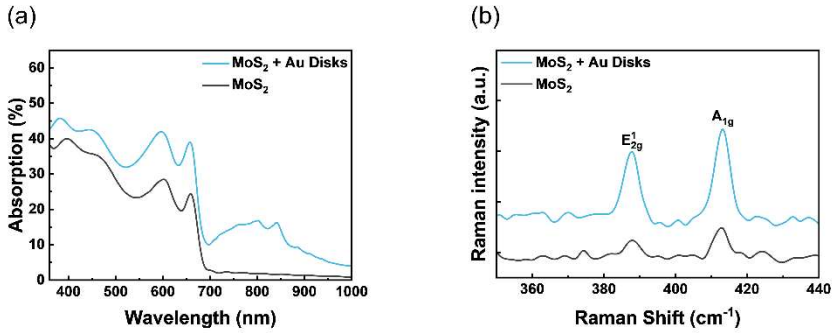

Fig. 2 Simulated extinction spectra and Raman spectroscopy. (a) Extinction spectra of MoS_2 with and without Au disk arrays. (b) Raman spectroscopy of MoS_2 with and without Au disk arrays.

Fig. 3(a-e) shows the output characteristics (I_{ds}-V_{ds}) of the device under dark conditions and illumination at different wavelengths, including 405 nm, 532 nm, 635 nm, 808 nm, and 1064 nm. All measurements were performed under ambient conditions at room temperature with a bias voltage ranging from -1.0 V to 1.0 V.

Under dark conditions, the device exhibits a low dark current I_{dark}, indicating that the h-BN tunneling layer effectively suppresses direct charge transport between the Au disk arrays and MoS_2 [30, 31]. Upon illumination, the photocurrent increases significantly, with distinct wavelength-dependent photoresponses.

In the 405-635 nm range, the photocurrent exhibits response behavior correlated with plasmonic resonance characteristics. The most pronounced photocurrent enhancement occurs within the wavelength range of 500-700 nm, which coincides with the broadband resonance peak of the Au disk arrays. This observation is consistent with the broadband resonance enhancement of the Au disk arrays in the visible range shown in Fig. 2a, demonstrating that the plasmonic resonance most effectively enhances the device's optoelectronic performance within its resonance band [16, 17].

Notably, in the near-infrared region (808 nm and 1064 nm), the device still exhibits detectable photoresponse, albeit with reduced photocurrent amplitude compared to the visible range. This phenomenon can be attributed to the contribution of the plasmonic hot electron injection mechanism: for photons with energies below the bandgap of MoS_2, hot electrons generated by non-radiative decay of plasmons can tunnel through the h-BN layer into the conduction band of MoS_2, thereby generating photocurrent [22-24]. This result confirms the effectiveness of the plasmonic enhancement strategy in extending the response bandwidth of two-dimensional materials [26, 29].

To further evaluate the dynamic performance of the device under modulated light conditions, we conducted time-dependent photoresponse measurements in the wavelength range of 405-808 nm, with the results presented in Fig. 4(a-d), which shows the time-dependent photocurrent (I-T) curves of the device with Au disk arrays under periodic on-off illumination at 405, 532, 635, and 808 nm, measured at a bias voltage of V_{ds} = -1 V. The device exhibits stable and reproducible switching behavior at all wavelengths, with no significant degradation over multiple cycles, indicating excellent operational stability and reliability [30, 34]. Under 635 nm illumination (Fig. 4c) at a power density

ISSN: 2414-1895 DOI: 10.6919/ICJE.202603_12(3).0011

of 238.43 mW/cm^2, the device demonstrates stable and fast photoswitching response, with rise/fall times of 40 ms/138 ms.

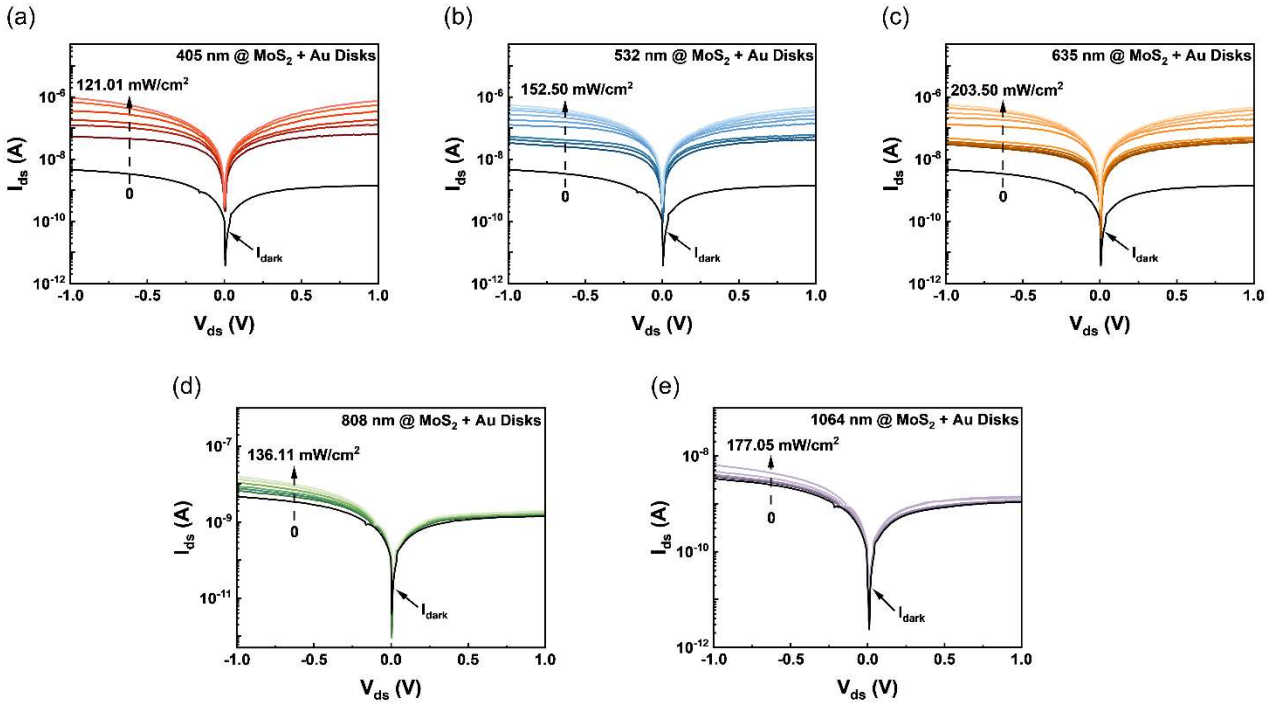

Fig. 3 I-V characteristics of the device at different wavelengths. (a-e) I-V curves measured under dark conditions and under illumination at 405, 532, 635, 808, and 1064 nm.

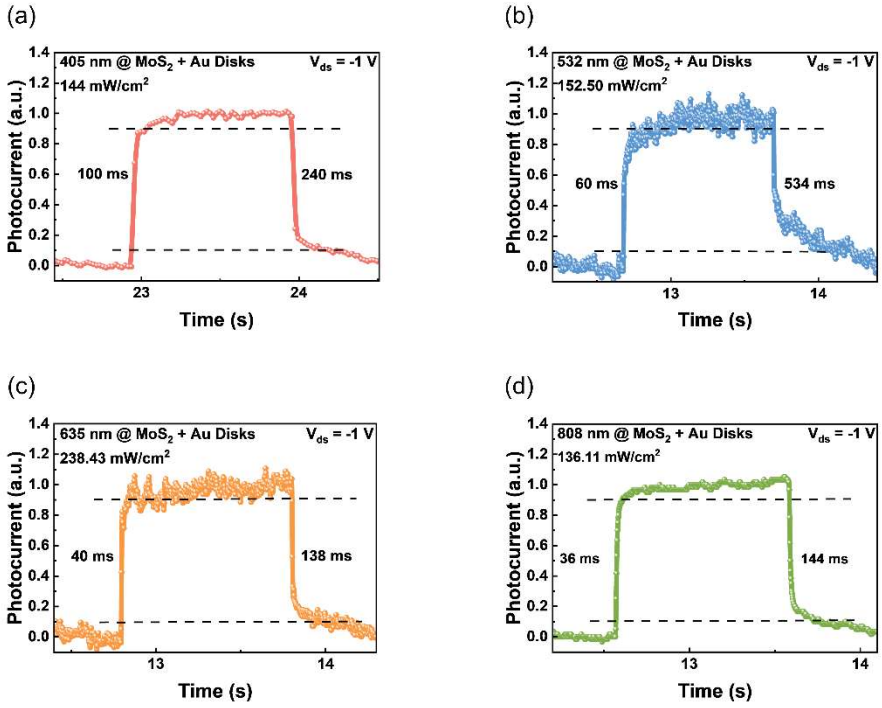

Fig. 4 Temporal response characteristics of the device (V_{ds} = -1 V). (a-d) Photoswitching response curves under illumination at 405, 532, 635, and 808 nm.

ISSN: 2414-1895 DOI: 10.6919/ICJE.202603_12(3).0011

Fig. 5(a-d) presents the responsivity (R) and detectivity (D*) of the device as functions of incident power density under illumination at 405, 532, 635, and 808 nm. At all measured wavelengths, both R and D* decrease monotonically with increasing power density, which is attributed to photocarrier saturation effects [9, 33]. At a low power density of 0.1 mW/cm^2, the responsivity under 405, 532, and 635 nm illumination reaches relatively high levels (in the range of 200-1000 A/W), with comparable values across these three wavelengths; the responsivity at 808 nm is comparatively lower. The high performance at 532 nm and 635 nm originates from the localized electric field enhancement effect of the Au disk arrays [16, 21], while the response at 808 nm is primarily governed by the hot electron injection mechanism [22, 24]. Although 405 nm lies away from the resonance peak, it still exhibits appreciable response, which may be associated with the intrinsic absorption of MoS_2 and weak enhancement effects [6, 17]. When the power density increases to 1000 mW/cm^2, the responsivity at all wavelengths converges to the same order of magnitude. The results in Fig. 5(a-d) demonstrate that the device achieves effective plasmonic enhancement across the visible to near-infrared spectral range.

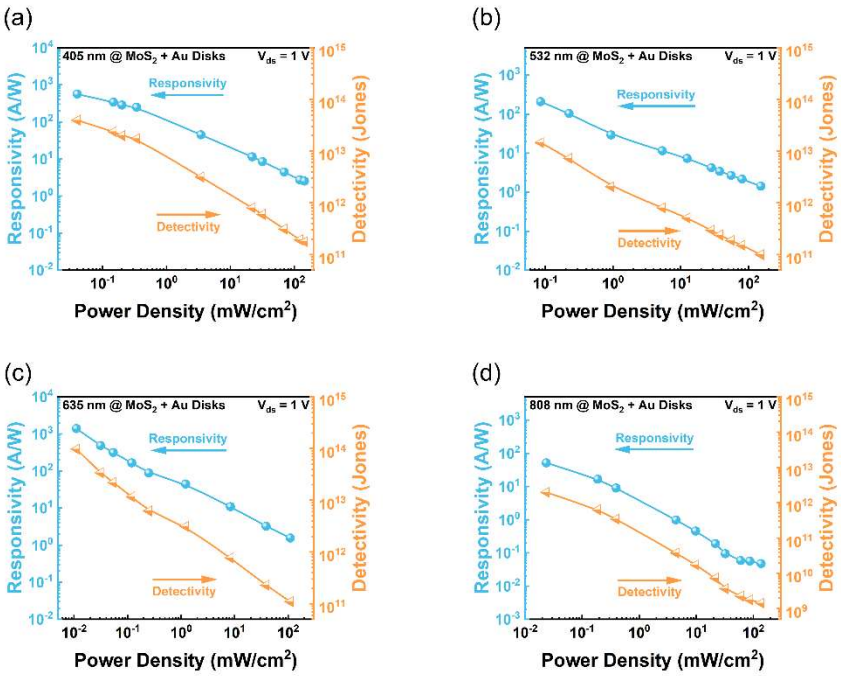

Fig. 5 Responsivity (R) and detectivity (D*) of the device as functions of incident power density. (a-d) R and D* under illumination at 405, 532, 635, and 808 nm, respectively. Both R and D* decrease with increasing power density.

Fig. 6(a-d) presents a comparison of the responsivity (R) and detectivity (D*) as functions of power density for devices with and without Au disk arrays under illumination at 405 nm, 532 nm, 635 nm and 808 nm. It can be observed that both R and D* of the device with Au disk arrays are higher than those of the reference device without Au disk arrays at all wavelengths, confirming the plasmonic enhancement effect of the Au disk arrays [16, 29]. In the low power density region, the responsivity of the device with Au disk arrays is significantly improved compared to the device without Au disk arrays, which is consistent with a mechanism dominated by plasmonic near-field enhancement [16, 21]; the enhancement in the 808 nm band is primarily attributed to the contribution of hot electron injection [22, 24]. Regarding detectivity, the device with Au disk arrays exhibits a higher level of performance, whereas the response of the device without Au disk arrays mainly originates from the intrinsic absorption of MoS_2, with its performance being noticeably limited in the near-infrared region,

ISSN: 2414-1895 DOI: 10.6919/ICJE.202603_12(3).0011

consistent with the bandgap characteristics of MoS_2 [6, 10]. The results in Fig. 6(a-d) validate the core role of the Au disk arrays in enhancing device performance.

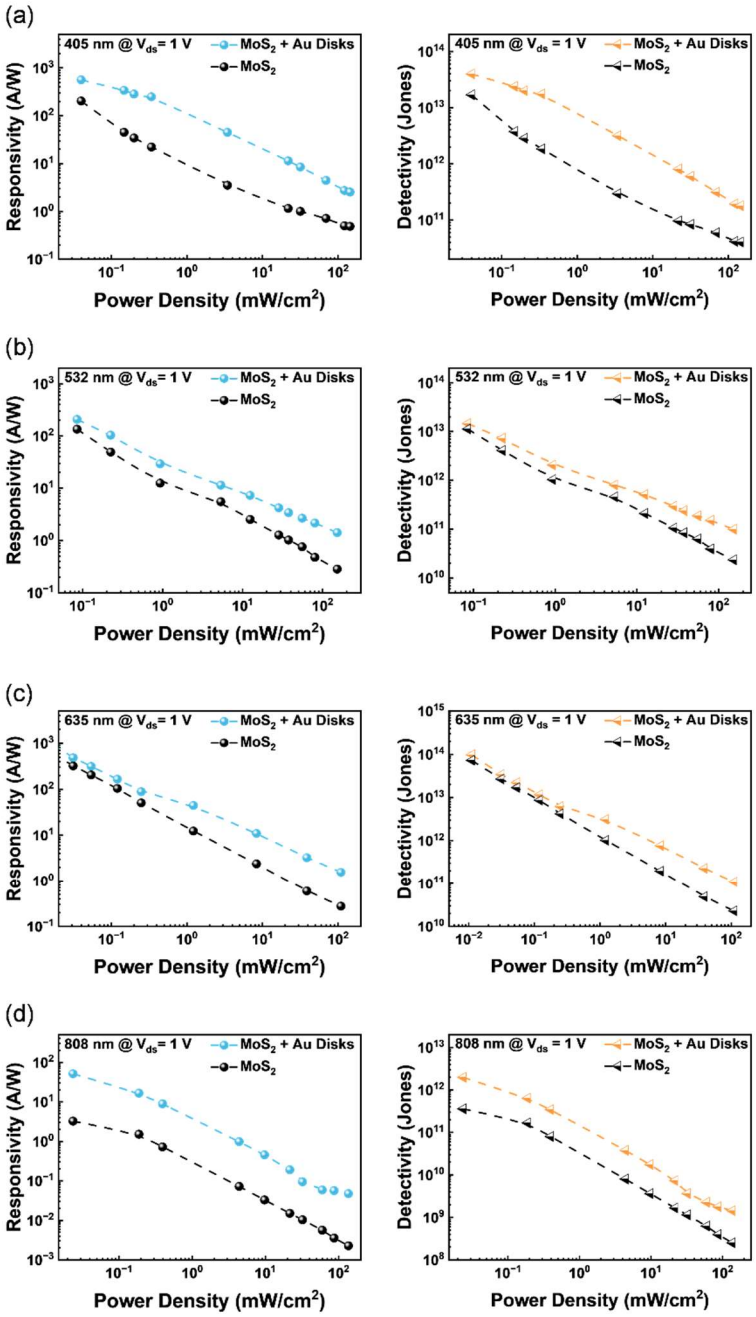

Fig. 6 Performance comparison of devices with and without Au disk arrays. (a-d) Comparison of R and D* under illumination at 405, 532, 635, and 808 nm for devices with and without Au disk arrays.

In summary, the performance enhancement of our device can be attributed to the synergistic interplay of three mechanisms. First, in the near-field optical enhancement mechanism, FDTD simulations confirm that the Au disk arrays generate localized electric field enhancement at the resonance wavelength, boosting light absorption in MoS_2 [16, 17, 20]. This enhancement effect is particularly pronounced for few-layer MoS_2 with a thickness of 20-30 nm, as the thicker material can accommodate a greater number of photogenerated carriers [8, 9]. Second, in the hot electron tunneling injection mechanism, the work function of Au (~ 5.1 eV) and the electron affinity of MoS_2 (~ 4.0 eV)

ISSN: 2414-1895 DOI: 10.6919/ICJE.202603_12(3).0011

form a Schottky barrier of approximately 1.1 eV [8]. The monolayer h-BN (bandgap ~ 6 eV, electron affinity ~ 0 eV) creates a triangular potential barrier [30, 31]. Under illumination, the relaxation of plasmons generates hot electrons with energies above the Au Fermi level, which can tunnel through the h-BN layer into the conduction band of MoS_2, contributing additional photocurrent [22, 23, 32]. Simultaneously, h-BN suppresses electron injection in the dark state, maintaining a low dark current [30, 31]. Third, in the strain effect mechanism, the redshift of characteristic Raman peaks indicates the presence of tensile strain in MoS_2 [25, 26]. According to literature reports, this strain induces bandgap narrowing, thereby extending the long-wavelength response range of the device [25-27]. This mechanistic framework is consistent with recent reports on plasmon-enhanced two-dimensional material photodetectors [26, 29], validating the effectiveness of the h-BN tunneling layer structure.

3. Conclusion

In this work, we have demonstrated a plasmon-enhanced photodetector based on few-layer MoS_2 integrated with direct writing lithographically patterned Au disk arrays and a monolayer h-BN tunneling layer, achieving broadband spectral response from 405 nm to 1064 nm. Through plasmonic enhancement effects and interfacial synergy, the device exhibits a maximum responsivity of 1384 A/W and a detectivity of 9.73×10^{13} Jones under 635 nm illumination. Time-resolved photoresponse measurements reveal stable modulation behavior in the visible range with millisecond-scale response times. Compared with devices without Au disk arrays, the plasmonic structure not only significantly enhances the photocurrent amplitude but also effectively broadens the spectral response range. Finite-difference time-domain simulations confirm pronounced electric field enhancement at the MoS_2 layer induced by the Au disk arrays. Band structure analysis demonstrates that the h-BN tunneling layer effectively suppresses dark current while facilitating hot electron injection. In summary, the few-layer MoS_2 plasmon-enhanced photodetector based on direct writing lithographically patterned Au disk arrays and an h-BN tunneling layer achieves systematic improvement in optoelectronic performance through plasmonic engineering, providing a viable structural strategy for high-performance visible light photodetection based on two-dimensional materials.

4. Experimental Section

Devices Fabrication: Devices were fabricated on double-side polished quartz substrates (1 cm × 1 cm). The substrates were sequentially cleaned by sonication in acetone, ethanol, and deionized water for 5 min each, dried with nitrogen gas, and baked on a hot plate at 150℃ for 5 min. Au disk arrays were fabricated by laser direct writing lithography: ARP-5350 photoresist was spin-coated at 4000 rpm for 60 s and baked at 105℃ for 4 min. After exposure, the patterns were developed using TMAH solution and rinsed with deionized water. A Ti adhesion layer (1 nm) and an Au layer (40 nm) were sequentially deposited by electron beam evaporation, followed by lift-off in acetone, yielding Au disk arrays with a diameter of 1.5 μm and a period of 2.5 μm.

Monolayer h-BN grown on copper foil was transferred onto the Au disk arrays using a PMMA-assisted wet transfer method: PMMA was spin-coated onto the h-BN/Cu substrate, and the Cu foil was etched using a CuCl solution. The PMMA/h-BN film was rinsed in deionized water and transferred onto the target substrate. After drying at 100℃, PMMA was removed with acetone. Subsequently, few-layer MoS_2 (20-30 nm thick) was dry-transferred onto the h-BN surface using a PDMS stamp and then heated at 90℃ for 5 min to ensure intimate contact.

Source and drain electrodes were defined by lithography, followed by electron beam evaporation of Ti/Au (10 nm/50 nm) and lift-off in acetone. Reference devices without Au disk arrays were fabricated on the same quartz substrate following identical procedures.

Characterization and Measurements: Device morphology was examined using optical microscopy. Thickness and surface topography were characterized by atomic force microscopy (AFM). Raman spectra were acquired using a confocal Raman spectrometer with a 532 nm excitation laser.

ISSN: 2414-1895 DOI: 10.6919/ICJE.202603_12(3).0011

Optical simulations were performed using Lumerical FDTD Solutions. The simulation model included Au disks (diameter: 1.5 μm, period: 2.5 μm, thickness: 40 nm), a quartz substrate (refractive index: 1.5), and a 20 nm thick MoS_2 layer. A plane wave was normally incident over a wavelength range of 360-1000 nm, with periodic boundary conditions in the x-y directions and perfectly matched layer (PML) boundaries in the z-direction, using a grid size of 0.1 nm. Electric field distributions and extinction spectra (1 - R - T) were recorded.

Electrical measurements were performed using a probe station connected to a semiconductor parameter analyzer. Laser diodes at 405, 532, 635, and 808 nm with tunable power were used as light sources, with a spot diameter of approximately 1 mm. Power density was calibrated using a power meter. All measurements were performed under ambient conditions at room temperature.

References

[1] A. Elbanna, H. Jiang, Q. Fu, et al., 2D Material Infrared Photonics and Plasmonics. ACS Nano, 2023. 17(5): p. 4134–4179.

[2] C. Wang, Q. Wu, Y. Ding, et al., High-Responsivity and Broadband MoS2 Photodetector Using Interfacial Engineering. ACS Applied Materials & Interfaces, 2023. 15(39): p. 46236–46246.

[3] X. Li, J. ZhuB. Wei, Hybrid nanostructures of metal/two-dimensional nanomaterials for plasmon-enhanced applications. Chemical Society Reviews, 2016. 45(11): p. 3145–3187.

[4] J. An, X. Zhao, Y. Zhang, et al., Perspectives of 2D Materials for Optoelectronic Integration. Advanced Functional Materials, 2022. 32(14).

[5] J. Zha, M. Luo, M. Ye, et al., Infrared Photodetectors Based on 2D Materials and Nanophotonics. Advanced Functional Materials, 2022. 32(15).

[6] N. Goel, A. Kushwaha, S. Agarwal, et al., A critical review of recent advances, prospects, and challenges of MoS2/Si heterostructure based photodetectors. Journal of Alloys and Compounds, 2025. 1010.

[7] Y. Wang, G. Zhou, Z. Zhang, et al., Graphene-, Transition Metal Dichalcogenide-, and MXenes Material-Based Flexible Optoelectronic Devices. Nanomaterials, 2025. 16(1).

[8] W. Wang, X. Zeng, J. Warner, et al., Photoresponse-Bias Modulation of a High-Performance MoS2 Photodetector with a Unique Vertically Stacked 2H-MoS2/1T@2H-MoS2 Structure. ACS Applied Materials & Interfaces, 2020. 12(29): p. 33325–33335.

[9] X. Xu, R. Duan, W. Qi, et al., Manipulating Carrier Behavior by the Size Effect of Decoration in MoS2 Photodetectors. Advanced Optical Materials, 2025. 13(6).

[10] O. Yi, C. Zhang, J. Wang, et al., Gate-Tunable Dual-Mode Optoelectronic Device for Self-Powered Photodetector and Optoelectronic Synapse. Advanced Science, 2025. 12(17).

[11] J. Zou, Y. Huang, W. Wang, et al., Plasmonic MXene Nanoparticle-Enabled High-Performance Two-Dimensional MoS2 Photodetectors. ACS Applied Materials & Interfaces, 2022. 14(6): p. 8243–8250.

[12] P. Vashishtha, I. Abidi, S. Giridhar, et al., CVD-Grown Monolayer MoS2 and GaN Thin Film Heterostructure for a Self-Powered and Bidirectional Photodetector with an Extended Active Spectrum. ACS Applied Materials & Interfaces, 2024. 16(24): p. 31294–31303.

[13] C. YanH. Liu, Multifunctional Phototransistor Based on MoS2/Ta2NiSe5/WSe2 vdW Heterojunctions with High-Performance Anti-Ambipolar Transport. Advanced Optical Materials, 2026. 14(4).

[14] K. Ponnusamy, J. Bong, H. Lee, et al., Promoter-Free Synthesis of Wafer-Scale Monolayer MoS2 for Visible to Near-Infrared Photodetection. ACS Applied Materials & Interfaces, 2026. 18(1): p. 1995–2008.

[15] W. WangL. Qi, Light Management with Patterned Micro- and Nanostructure Arrays for Photocatalysis, Photovoltaics, and Optoelectronic and Optical Devices. Advanced Functional Materials, 2019. 29(25).

[16] J. Miao, W. Hu, Y. Jing, et al., Surface Plasmon-Enhanced Photodetection in Few Layer MoS2 Phototransistors with Au Nanostructure Arrays. Small, 2015. 11(20): p. 2392–2398.

[17] J. Guo, S. Li, Z. He, et al., Near-infrared photodetector based on few-layer MoS2 with sensitivity enhanced by localized surface plasmon resonance. Applied Surface Science, 2019. 483: p. 1037–1043.

[18] S. Ghopry, S. Alzahrani, B. Liu, et al., Dimensionally controlled MoS2 nanodiscs for optimal localized surface plasmonic resonance in nanohybrid photodetectors. Nano Express, 2025. 6(4).

ISSN: 2414-1895 DOI: 10.6919/ICJE.202603_12(3).0011

[19] Y. Liu, R. Cheng, L. Liao, et al., Plasmon resonance enhanced multicolour photodetection by graphene. Nature Communications, 2011. 2.

[20] R. Xing, X. Zhang, X. Fan, et al., Coupling Strategies of Multi-Physical Fields in 2D Materials-Based Photodetectors. Advanced Materials, 2025. 37(16).

[21] L. Liu, Y. Guo, H. Shang, et al., Visible-Blind Spectrally Selective Near-Infrared Photodetection with Enhanced Sensitivity. ACS Applied Materials & Interfaces, 2025. 17(49): p. 66956–66964.

[22] T. Fayad, M. Eisa, E. Salih, et al., Self-biased visible-NIR photodetection enabled via a dual-heterojunction n-MoS2/p-CuO/n-Si design. Materials Advances, 2026. 7(2): p. 1265–1271.

[23] Y. Huang, C. Chen, C. Huang, et al., Flexible 2D material hetero-structure photodetectors with high responsivities, tunable wavelengths and short response times. 2D Materials, 2026. 13(1).

[24] D. Sahu, S. DasS. Ray, Plasmonic Au/MoxW1-xS2/Si Heterojunction for Broadband Photodetection. ACS Applied Materials & Interfaces, 2026. 18(1): p. 2109–2121.

[25] Z. Peng, X. Chen, Y. Fan, et al., Strain engineering of 2D semiconductors and graphene: from strain fields to band-structure tuning and photonic applications. Light: Science & Applications, 2020. 9(1).

[26] D. Lu, Y. Chen, L. Kong, et al., Strain-Plasmonic Coupled Broadband Photodetector Based on Monolayer MoS2. Small, 2022. 18(14).

[27] X. Hu, J. Li, H. Ji, et al., Achieving dark current suppression and photocurrent enhancement simultaneously in 2D MoS2 photodetector via Ag nanocluster modification. Nano Research, 2026. 19(1).

[28] X. Zhou, Z. Weng, J. Li, et al., Enhanced Photoelectric Response in MoS2/Graphene Heterostructures via Surface Plasmon Resonance. ACS Applied Nano Materials, 2026. 9(2): p. 1195–1204.

[29] H. Dong, Q. Yin, Z. Wu, et al., Visible-near infrared broadband photodetector enabled by a photolithography-defined plasmonic disk array. Photonics Research, 2025. 13(2): p. 453–467.

[30] M. Zhang, G. Zeng, G. Wu, et al., Van der Waals integrated plasmonic Au array for self-powered MoS2 photodetector. Applied Physics Letters, 2023. 122(25).

[31] H. Wang, Z. Li, D. Li, et al., Van der Waals Integration Based on Two-Dimensional Materials for High-Performance Infrared Photodetectors. Advanced Functional Materials, 2021. 31(30).

[32] S. Roy, S. Aktar, A. Tamang, et al., 0D/2D Nanomaterials Heterostructures for High-Performance Photodetectors: Combining Quantum Dots With 2D Materials. Small, 2026.

[33] J. He, Y. Yang, Y. He, et al., Low Noise and Fast Photoresponse of Few-Layered MoS2 Passivated by MA3Bi2Br9.ACS Photonics, 2018. 5(5): p. 1877–1884.

[34] Q. Zhang, B. Zhao, J. Chen, et al., High-Speed, High-Responsivity on-Chip Monolayer MoS2 Photodetector at Telecom Wavelengths. ACS Photonics, 2026. 13(4): p. 913–919.